Influence of water level on RC caisson subjected to underwater explosions

Y. Zhang [a], Y.D. Zhou [b,**], H. Wu [b,*]

[a] *Institute of Defense Engineering, AMS, PLA, Beijing, 100850, China*
[b] *College of Civil Engineering, Tongji University, Shanghai, 200092, China*

A R T I C L E   I N F O

A B S T R A C T

With the increasing significance of marine safety issues, the studies on the underwater blast-resistant performance of wharves, e.g., reinforced concrete (RC) caissons, has become an urgent demand. At present, the influence of water level on caisson subjected to underwater explosions was studied experimentally and numerically, e.g., underwater explosion loading characteristics and dynamic behaviors of caisson. Firstly, four shots of underwater explosion test were carried out both in free field and on a partially submerged caisson specimen, and the overpressure- and deflection-time histories, as well as the structural damage pattern were recorded. Then, the underwater explosion loading characteristics including the preceding blast wave and the succeeding bubble oscillations, the cut-off effect of the water surface, as well as the dynamic behaviors of caisson are comprehensively discussed. Furthermore, both the 1D and 3D finite element (FE) models were established, and by adopting Coupled Eulerian-Lagrangian method and remapping technology, the reliability of the FE models and analysis approach were validated by comparing with the test results. Finally, the influence of water level on the dynamic behaviors of caisson against underwater explosions were numerically examined. It derives that, the empirical formula derived based on spherical charge for underwater explosion peak overpressure is applicable to group charge, while the formula for impulse provides higher prediction on group charge; bubble oscillation has great influence on the impulse of underwater explosions; the unsubmerged part of hydraulic structures suffers slighter damage during underwater explosions than submerged part; the upper part of caisson is more sensitive to the change of water level; the partially submerged caisson shows better blast-resistant performance than fully submerged caisson. The present work could provide helpful reference for the studies on the underwater explosion loadings, as well as the blast-resistant assessment and design of hydraulic structures.

1. Introduction

Taking great responsibilities for national defense and economy, the wharf is one of the most critical structures in coastal engineering for both military and civil purposes, and consequently under high risk of being targeted by intentional and accidental attacks. Specifically, for the common structural form of wharves, the reinforced concrete (RC) caisson quay wall is under threat of potential underwater explosions caused either by direct or accompanying assaults. Therefore, it is significant to study the underwater blast-resistant performance of RC caisson to propose effective suggestions for protective design. It should be noted that, the water level commonly varies due to the tidal change and berthing situation, which yields different submerging scenarios, e.g., partial, shallow and deep submersion. Since the propagation of underwater blast wave as well as the motion of fluid field differ tremendously between

water and air, the underwater explosion loading distribution on hydraulic structures is greatly affected by the water level. Accordingly, the dynamic behaviors of caisson under different submerging scenarios may show dissimilarities, and relevant research needs to be conducted to investigate the influence of water level on the dynamic behaviors of RC caisson subjected to underwater explosions.

The research on underwater explosion has been developing for over a century, and many valuable results and conclusions have been derived. Among them, the study on the dynamic behaviors of structures against underwater explosion must be based on the understanding of explosion loading and its distribution on the target. Underwater explosion is a complex phenomenon, mainly including the preceding blast wave caused by charge detonation, and the succeeding bubble oscillation caused by the motion of detonation products, which has been studied both in free field and on structures. For the free field explosion scenarios,

one of the most influential achievements, e.g., the formulas for calculating overpressure and impulse of blast wave, were proposed by Cole (1948) through summarization of mainstream analytical theories and large amounts of test data, and refined by later discussions (Zamyshlyaev and Yakovlev, 1967; Liu, 2002). As for the loading characteristics under explosion scenarios with structure, the major concern is about the reflection characteristics of the underwater blast wave, as well as the evolution of bubble morphology. Taking the reflection coefficient proposed by Ben-Dor (1992) as the indication, Taylor (1963) analyzed the ideally oblique reflection of underwater blast wave on a rigid flat surface, while Zamyshlyaev and Yakovlev (1967) focused on the gravel and sandal surfaces. Gu et al. (2006) measured the reflected overpressure-time history on concrete frustums under near-field underwater explosions with JHL23 charge explosive, and determine the oblique reflection coefficients of underwater blast wave. Zhuang et al. (2020) conducted underwater explosion test with TNT explosive on partially submerged steel pipe piles, and recorded the reflected and diffracted overpressure-time histories at different height of pile specimens on the front and rear surfaces, respectively. As the distinctive feature of underwater explosion, the bubble oscillation has been thoroughly investigated theoretically and numerically for its period and motion patterns (Snay, 1956; Geers and Hunter, 2002). Besides, the geometric and kinematic characterizes, especially the cavitation effect of underwater explosion bubbles near various boundaries, e.g., free water surface and rigid surface (Li et al., 2020), as well as sandwich structure (Rolfe et al., 2020), have been discussed numerically by coupling the Runge-Kutta discontinuous Galerkin, boundary element and finite element (FE) methods, as well as an isentropic one-fluid cavitation model.

The clarification of underwater explosion loading characteristics and distribution laws has prompted studies on the dynamic behaviors of submarine structures. However, most studies in this field were originally intended for maritime affairs and Naval defense, which mainly concern the movable and floating structures, e.g., ships and submarines (Murata et al., 2004; Rajendran and Narasimhan, 2006; Hung et al., 2009; LeBlanc and Shukla, 2011). Having different material property and structural form, relatively few studies were carried out on the fixed and submerged structures, i.e., hydraulic RC facilities. For the basic structural member, e.g., RC slabs, Yang et al. (2019) and Zhao et al. (2018) conducted numerical simulations with the hybrid model combining smoothed particle hydrodynamics, Lagrange and Euler solvers to examine and compare the dynamic responses of RC slabs subjected to air and underwater explosions, indicating that the underwater explosion scenarios induce more severe damage to the slab. Another high concerning structure is the dam, which intercepts and blocks water for rivers and reservoirs. Since the actual scale dimension of the dam is exceedingly larger than common test sites, Huang et al., 2022a, 2022b utilized the centrifuge test to realize the near-field explosion effect for gravity dam. Combined with numerical simulations adopting Coupled Eulerian-Lagrangian method, the dynamic responses and failure modes of gravity dam subjected to underwater explosions were further analyzed for the influences of gravity acceleration, charge weight, and standoff distance. For the wharf structures, Zhuang et al. (2020) studied the damage modes of high pile wharves by performing multiple shots of underwater explosion test on partially submerged single RC piles with the height of 2.5 m and diameter of 100 mm. The failure modes, i.e., bending, bending-shear, and punching, were realized according to the range of scaled standoff. This test was further numerically simulated and discussed by Yan et al. (2020) and Tian et al. (2021). Regarding the target of the present work, i.e., the caisson structure, relevant investigations in open literature are comparatively insufficient. Dong et al. (2019) conducted the near-field and contact underwater explosion tests on RC caisson specimen with the dimension of 2980 mm × 1620 mm × 2190 mm, and further established the corresponding FE model with the explicit dynamic program LS-DYNA to evaluate the damage effect of the caisson. It shows that, the underwater explosions can cause serious damage to almost all components of the caisson gravity wharf, except for the bottom plate. Liu et al. (2020) further studied the contact explosion test scenarios in Refs (Dong et al., 2019). through numerical simulations, and pointed out that the failure of the front wall was basically formed during the impact phase of blast wave, while the side walls and top plate suffered more damage caused by bubble oscillation.

The variation of water level is inevitable for hydraulic structures, and its influence on the dynamic behaviors of structures subjected to underwater explosions needs to be examined. Li et al. (2018) numerically assessed the protective performance of a typical gravity dam against underwater explosions with five different water levels, and suggested that the dam exhibits better blast-resistant performance when the water level is below the change in downstream slope of dam. Besides, the simulation results of Liu et al. (2020) also indicated that the superstructure of the caisson above the water level remained almost intact after the underwater explosions, while the major part of the structure submerged in water was significantly damaged.

It should be noted that, the existing studies on RC structure subjected to underwater explosions is relatively scarce, and mainly reflected on: (i) the dam is taken as the target of most research, which could not represent the majority of hydraulic structures, especially for the caisson, in terms of the structural form, function and construction layout; (ii) for the wharf structures, the purpose of relevant studies are unclear with incomprehensive test data, the systematic discussion and conclusion have not been formed; (iii) the research on dynamic behavior of caisson structure is still insufficient in quantitative analysis, and the blast-resistant performance under various water levels is hardly involved. To address the above issues, at present, the influence of water level on the dynamic behaviors of caisson subjected to underwater explosions is examined both experimentally and numerically. Firstly, four shots of underwater explosion test were conducted with 0.2–1.0 kg TNT group charges (two shots in free field and two shots on a partially submerged RC caisson specimen), and the overpressure- and deflection-time histories were recorded in the test. Secondly, the refined FE models were established with the FE program AUTODYN (Southpointe, 2020), and the validation of the adopted material models and FE analysis approach was evaluated by comparing with the test data. Moreover, the explosion scenarios were numerically extended to different water levels, and the loading characteristics and dynamic behaviors of caisson against underwater explosions were discussed. The present study could provide useful suggestions for the blast-resistant assessment, design and layout of RC caisson wharves.

2. Underwater explosion test

In this section, total four shots of underwater explosion test were carried out, two of which were conducted in free field to survey the loading characteristics, while the other two were performed on a partially submerged RC caisson specimen to examine its dynamic behaviors under the impact of underwater explosions.

2.1. Test setup

As shown in Fig. 1, the test was conducted in a circular explosion test pool (10 m in diameter and 10 m in depth) with steel plates wrapped around the side and bottom, and the water depth was kept at 3.08 m for all four shots. A bridge truss for vertically suspending the charge and devices is set across the pool upon two track rails, which allows the bridge truss to move horizontally and cover the whole area of the pool. After two shots of test in free field, a 1/4 reduced scale caisson specimen (2800 mm × 2200 mm × 3540 mm) was placed in the pool for the other two shots. The specimen consists of a bottom plate, a top plate, a front wall, a rear wall, two side walls and inner partitions, which formed the structure of a 2 × 2 caisson unit with four chambers, as shown in Fig. 2. The cubic compressive strength of the concrete is 38.1 MPa and the specimen was set against one side of the pool to simulate the actual
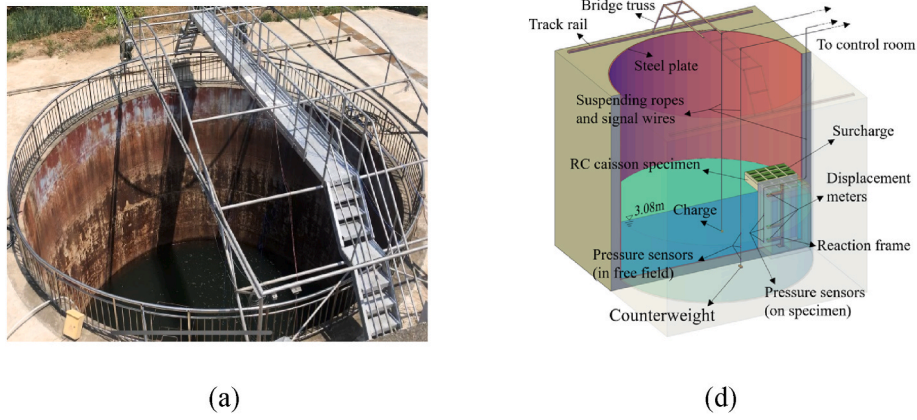
(a)   (d)

Fig. 1. Underwater explosion test setup (a) photograph (b) schematic.

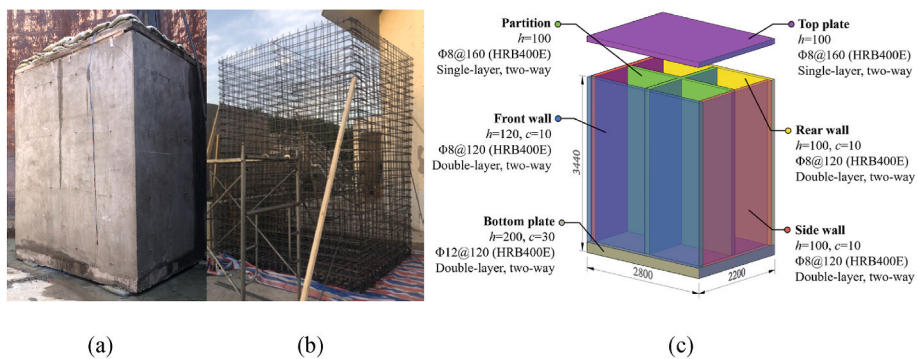(a)   (b)   (c)

Fig. 2. RC caisson (a) specimen (b) reinforcement cage (c) configuration and detailing (unit: mm).

situation that the caisson leans on the coast, with 1.5 t of sandbags piled upon the top plate as the surcharge.

As for the test measurements, Fig. 3(a and b) illustrates the layout of the sensoring instruments for both the explosion tests in free field and on caisson specimen, respectively. The overpressure- and deflection-time histories were recorded by utilizing the PCB Model W138A25 pressure sensors and JWS3C displacement meters, respectively. The PCB pressure sensor is a voltage sensor comprised of a precise element in a flexible transparent tube filled with silicone oil, which is specially designed for underwater measurement with the measuring range of 172 MPa, sensitivity of 0.03 mV/kPa, and sampling frequency of 1 MHz. The JWS3C displacement meter is waterproof and applicable to underwater test, which functions within the measuring range of 100 mm and under the sampling frequency of 200 kHz. During the first two shots in free field, as shown in Fig, 3(a), a group charge and three pressure sensors were positioned on two suspending ropes spaced apart at a horizontal

distance L, and 1 kg of counterweight was employed to reduce the sway of the suspending rope and stabilize the pressure sensors. For the other two shots on the caisson specimen, as shown in Fig. 3(b), three pressure sensors were fixed with steel wires on the exterior surface of front wall, while the displacement meters were installed in the chamber with a steel reaction frame to record the deflections of front wall. Besides, the explosives adopted in the present test are TNT group charges with the density of 1.6×10^3 kg/m^3.

Table 1 gives the test scenarios. After the successive test of Shot 1 and Shot 2, the water in the pool was drained in order to install the caisson specimen along with the sensors, and the pool was then refilled to the identical water level of 3.08 m. Shot 3 and Shot 4 were also carried out consecutively with the charge aligned horizontally to the middle of the chamber on one side as shown in Fig. 3(b).
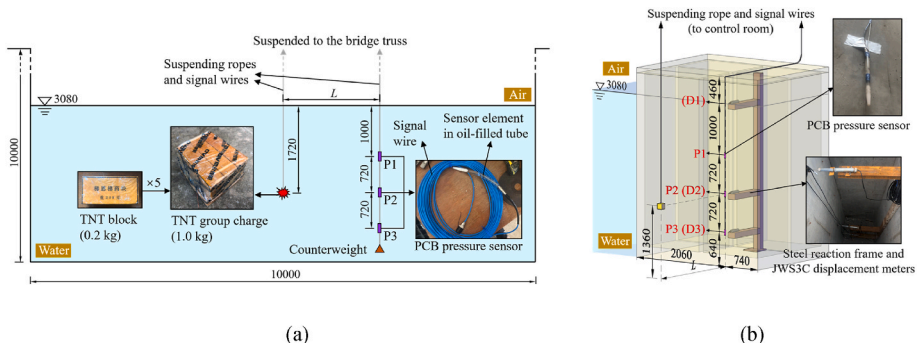

(a)   (b)

Fig. 3. Layout of test instruments (a) in free field (b) on caisson specimen (unit: mm).

Table 1

Underwater explosion test scenarios.

Scenario	Shot	Charge weight (kg)	L (m)	Scaled standoff (m/kg$^{1/3}$)
Free field	1	1	3.0	3.00
	2	1	0.8	0.80
Caisson specimen	3	0.4	2.0	2.71
	4	0.2	0.8	1.37

2.2. Loading characteristics

The research on the dynamic behaviors of caisson subjected to underwater explosions must be based on the understanding of corresponding loading characteristics. In this section, the underwater explosion loadings both in free field and on the caisson specimen are discussed by analyzing the test data, and comparing with the existing theories, e.g., the calculation formulas for peak overpressure and impulse in free field underwater explosion. The total of twelve overpressure-time histories were obtained from the present test, as shown in Fig. 4, the peak overpressure and the subsequent bubble oscillation can be clearly observed. Note that, the overpressure shown in Fig. 4(a and b) was detected in free field, which is essentially the incident overpressure; whereas the overpressures shown in Fig. 4(c and d) was measured on the RC caisson, which represents the superposition of incident and reflected overpressures on the surface of caisson specimen.

2.2.1. Peak overpressure

Fig. 4 shows the developing pattern of underwater explosion overpressure, i.e., sudden jump-decay-oscillation. When the blast wave front arrives, the overpressure increases almost instantaneously to the peak, and then decays rapidly to the equilibrium value near zero and remains, following by several bubble oscillations which appear in the form of comparably small periodic pressure fluctuations. The overpressure

induced by blast wave is the most threatening and concerned factor of underwater explosion loading, and the calculation formula given in Eq. (1) for underwater explosion peak overpressure in free field was first proposed by Cole (1948) and further improved by Zamyshlyaev and Yakovlev (1967).

$$P_m = \begin{cases} 44.1/Z^{1.5} & 6 < R/R_0 \le 12 \\ 52.2/Z^{1.13} & 12 < R/R_0 < 240 \end{cases} \tag{1}$$

where P_m is the peak overpressure; R is the standoff between the explosion center and the target; R_0 is the radius of equivalent spherical TNT charge; $Z = R/W^{1/3}$ is the scaled standoff; W is the equivalent TNT charge weight.

Fig. 5 compares the measured peak overpressures with the prediction curve of Eq. (1) according to the scaled standoff at each measuring point. It can be seen that the peak overpressures measured in free field test with group charges (Shot 1 and Shot 2) show good consistency with the predicted results, indicating that Eq. (1) derived based on spherical charge is also applicable to the group charge. Besides, due to the reflection effect on the specimen, the peak overpressures obtained from Shot 3 and Shot 4 are larger than Eq. (1) with a magnification factor between 1.2 and 1.6, which is consistent with the reflection law of underwater explosion drawn theoretically by Zamyshlyaev and Yakovlev (1967) and conclusion obtained experimentally by Zhuang et al. (2020).

2.2.2. Impulse

The overpressure caused by underwater explosion blast wave has the intensive loading characteristics with high peak value and short time duration. The structural dynamic response and damage level are dominated by both the explosion overpressure and impulse. Thus, in order to thoroughly evaluate the effect of underwater blast wave and bubble oscillation, the explosion impulse is discussed in this section. It should be pointed out that the impulse mentioned in the present work is actually the specific impulse, i.e., impulse per unit area, yet denoted simply
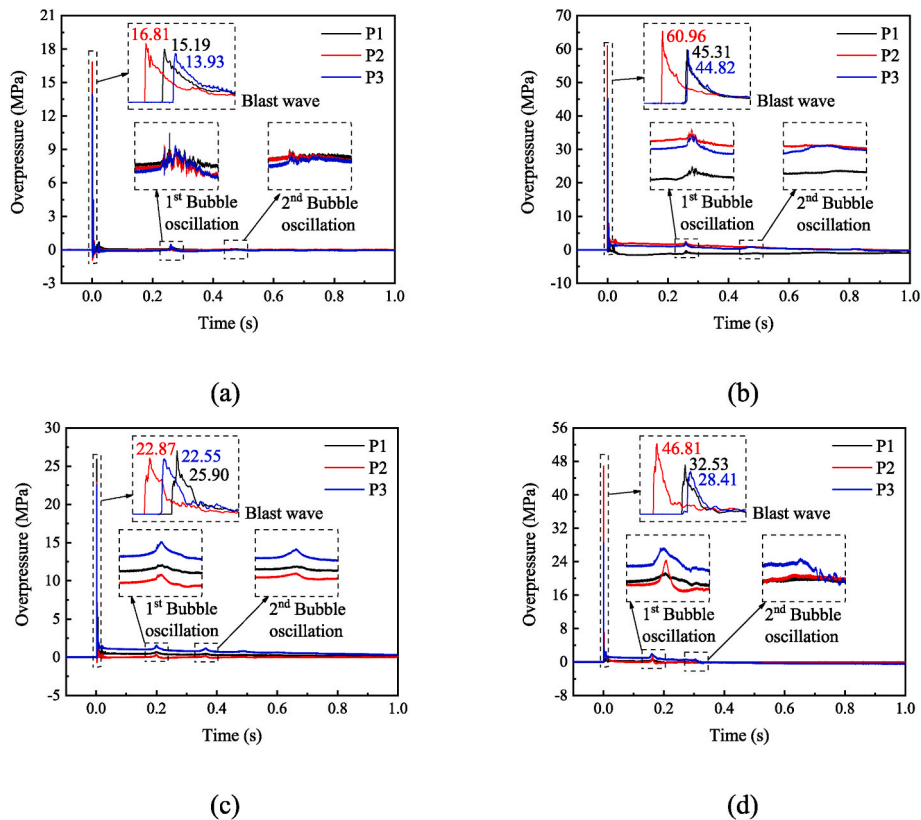

Fig. 4. Underwater explosion overpressure time-histories (a) Shot 1 (b) Shot 2 (c) Shot 3 (d) Shot 4.
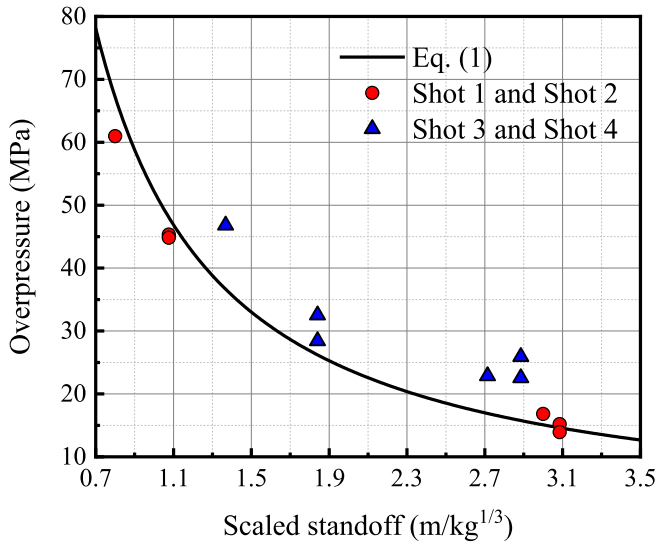
Fig. 5. Comparisons of peak overpressure according to the scaled standoff.

as 'impulse' for short following the convention in underwater explosion studies. Zamyshlyaev and Yakovlev (1967) proposed the calculation formula Eq. (2) for the impulse induced by free field underwater blast wave with the explosion depth less than 100 m. It should be emphasized that the applicability of Eq. (2) is limited to a very short time period (usually within 1 ms), which can only characterize the effect of underwater blast wave without the involve of bubble oscillations.

$$I = \begin{cases} P_m\theta(1 - e^{-t/\theta}) & 0 \leq t < \theta \\ P_m\theta[0.632 + 0.368 \ln(t/\theta)] & \theta \leq t < 10\theta \end{cases} \quad (2)$$

where I is the impulse; t is the time after the peak overpressure; θ is the time constant which represents the time duration for the overpressure to decay from P_m to P_m/e (e is the natural logarithm). Zamyshlyaev and Yakovlev (1967) proposed the formula for θ in far-field explosion through theoretical analysis, and Liu et al. (Liu, 2002) further supplemented the near-field range based on numerical simulations as

$$\theta = \begin{cases} 0.45R_0(R/R_0)^{0.45} \times 10^{-3} & R/R_0 \leq 30 \\ 3.5(R_0/c)\sqrt{\lg(R/R_0) - 0.9} & 30 < R/R_0 < 240 \end{cases} \quad (3)$$

where c is the sound speed in water, and the value can be taken as 1500 m/s.

The impulse I in Eq. (2) is the integral of instantaneous overpressure over time. Therefore, as shown in Fig. 6, the overpressure measured in the test is integrated over the corresponding time duration according to Eq. (3), and the result is compared with Eq. (2). It can be seen that the impulses derived from the test data exhibit an upward trend with gradually decreasing growth rate, which are basically in accordance with Eq. (2) with the time duration less than 10θ, i.e., the main loading time duration of underwater explosion blast wave without concern for bubble oscillation. For Shot 1 and Shot 2, the test results of impulse are slightly smaller than the predicted curves of Eq. (2), which implies that the group charge may produce a lower impulse than spherical charge with equal weight. For Shot 3 and Shot 4, the test results are similar or slightly higher compared with Eq. (2), which indicates that the underwater explosion impulse acting on the structure is larger than that in free field within 10θ due to the reflections of blast wave on the caisson. It should be pointed out that, obvious incoherence and sudden trend changes can be noted in curves of test results shown in Fig. 6(a), which is primarily owing to the accidental measuring errors.

However, the applicable range of Eq. (2) is limited within 10θ to inspect the effect of underwater blast wave, instead of the whole process of underwater explosion loading, i.e., cannot consider the bubble
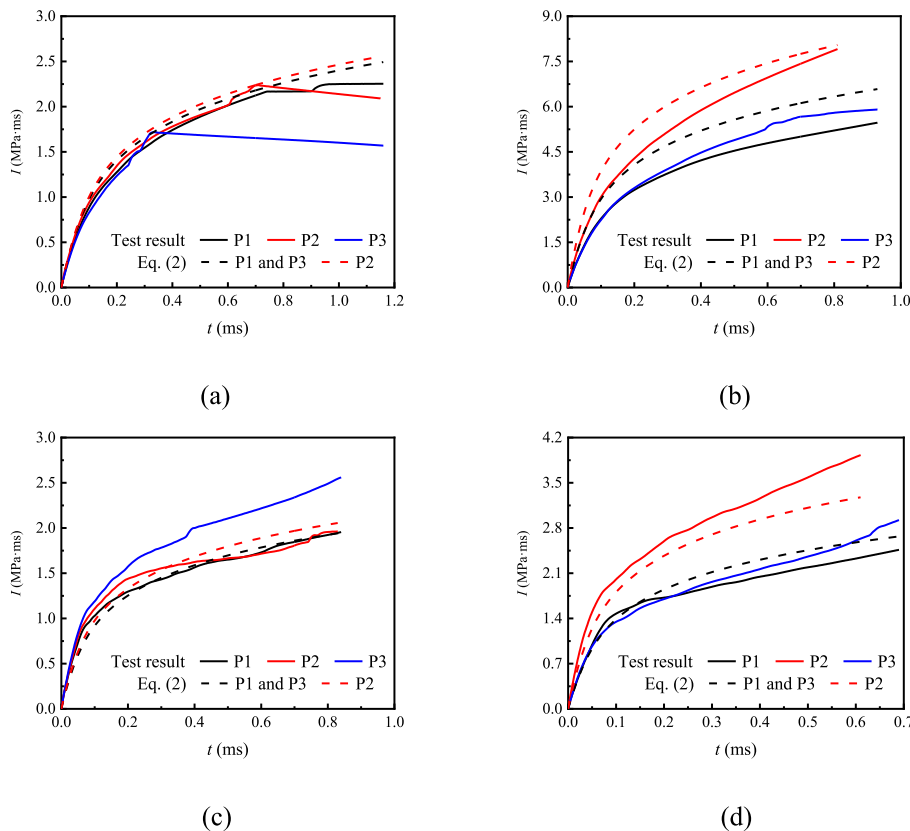

(a)

(b)

(c)

(d)

Fig. 6. Comparisons of blast wave impulse (a) Shot 1 (b) Shot 2 (c) Shot 3 (d) Shot 4.

oscillation. Although the overpressure value of bubble oscillation is remarkably low compared to the peak overpressure caused by blast wave, its duration time is evidently longer, which advances the requirement for examining its contribution in impulse. Fig. 7 shows the overpressure and its integration, i.e., impulse, of the present test within 1 s according to Fig. 4. It can be observed that the impulse-time history evolves in a stepped manner that each bubble oscillation is accompanied by a corresponding increase in impulse, which demonstrates the fact that the bubble oscillation cannot be neglected when analyzing the underwater explosion loading as well as the structural behaviors. It should be noted that, though counterweights were applied, the suspending ropes bound with sensors still wobbled slightly under the impact of explosion, resulting in the baseline offset of the overpressure-time histories, which can be observed in Fig. 4. In order to eliminate the error of impulse caused by baseline offset, the baselines of overpressure-time histories in Fig. 4 were rectified and illustrated in Fig. 7, and the corresponding impulses are integrated base on the adjusted data. Therefore, the specific value of impulse in Fig. 7 may not be perfectly accurate considering that the inevitable accidental error exists during the process of baseline adjusting, but the similarity of the impulse-time histories in the four shots indicates that: (i) the impulse caused by blast wave increases as the standoff decreases under the same charge weight; (ii) the final impulse of underwater explosion appears to be larger at lower measuring points, indicating that the bubble oscillation has a greater effect in deep water, the similar conclusions were also experimentally derived by Zhuang et al. (2020).

2.2.3. Cut-off effect

According to the propagation characteristics of the blast wave, when the blast wave reaches the interface between different media, the reflection and transmission will occur, and the overpressure of the reflected and transmitted wave is dependent on the impedance ratio between the two media. Since the impedance of air is significantly smaller than that of water, according to the reflection law of stress wave (Wang, 2005) given in Eq. (4), the underwater explosion blast wave produces a tensile wave when reflected at the water surface, i.e., the negative

overpressure since the impedance ratio between water and air is exceedingly larger than 1. For the measuring points near the water surface, the blast wave front sweeps and then reflected wave follows, thus the overpressure superposition of the two waves shows a steep drop in the time-history curve, namely the cut-off effect, as shown in Fig. 8. It can be seen that, during the decay of blast wave overpressure, the reflected wave with negative overpressure reaches the measuring point and forced a sudden drop to the overpressure time-history, and then gradually enters the positive phase. However, since the pressure sensors cannot correctly detect the negative pressure, the overpressure time-history remains at hydrostatic pressure during the negative phase. The time gap between the occurrence of peak overpressure and cut-off
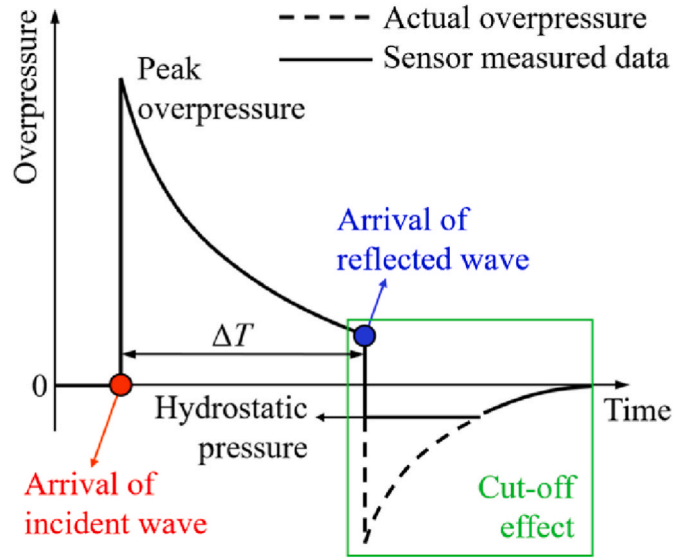

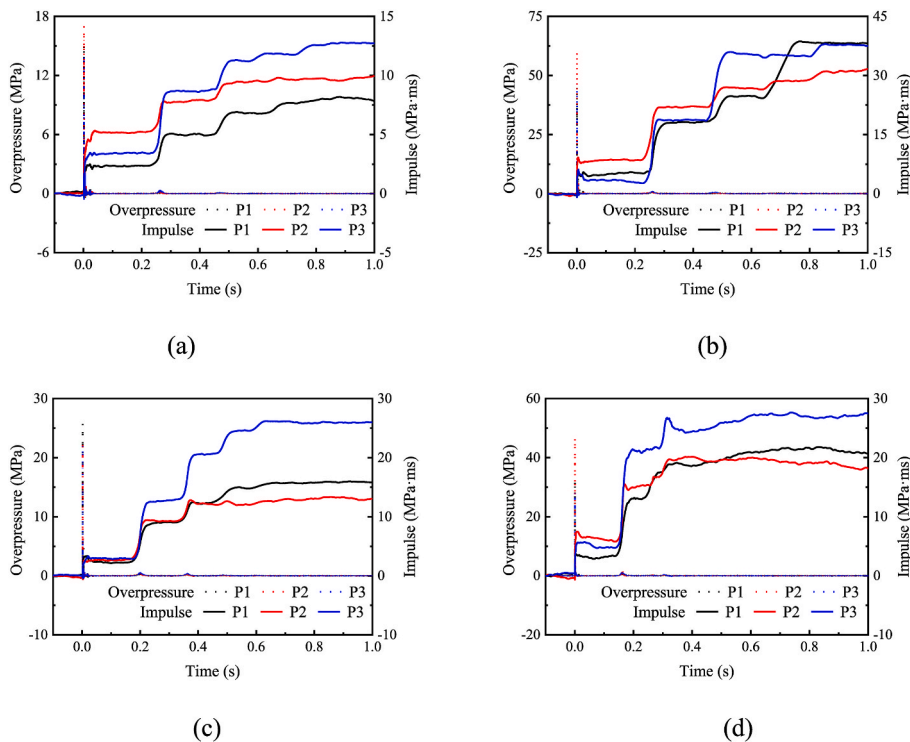**Fig. 8.** Schematic of cut-off effect on underwater explosion overpressure-time history.

(a)

(b)

(c)

(d)

Fig. 7. Impulse time-history (a) Shot 1 (b) Shot 2 (c) Shot 3 (d) Shot 4.

effect is denoted as ΔT.

$$\Delta \sigma_R = \frac{1-n}{1+n}\Delta \sigma_I; \quad \Delta \sigma_T = \frac{2}{1+n}\Delta \sigma_I; \quad v_R = -\frac{1-n}{1+n}v_I;$$
$$v_T = \frac{2}{1+n}v_I; \quad n = \frac{(\rho_0 C_0)_1}{(\rho_0 C_0)_2} \tag{4}$$

where $\Delta \sigma$ is stress; v is the velocity; the subscript I, R, T refer to incident, reflected and transmitted circumstances, respectively; n is the impedance ratio of medium 1 to medium 2; ρ_0 is the initial density; C_0 is the initial sound speed; the subscript 1 and 2 refer to the incident and transmitted media, respectively.

As shown in Fig. 9, similar trends can be observed at P1 measuring point (1 m underwater) in Shot 1 and Shot 2, and the ΔT in the two overpressure curves are 0.744 ms and 1.116 ms, respectively. The geometric diagram of the charge, measuring point and water surface (according to Cole (1948), the incident and reflection angles, i.e., α_I and α_R in the present test can be approximately assumed to be equal) is shown in Fig. 10. In which L is the horizontal distance; S is the distance; v is the velocity, T is the time duration, the subscript I, RI and RR refer to the incident wave, cut-off wave before reflection and cut-off wave after reflection, respectively. In order to ensure that the reason for the steep drops observed in Fig. 9 is the cut-off effect indeed, ΔT derived from the test data is compared with the corresponding calculation results given in Table 2, where the velocity of the incident wave is taken as 1500 m/s. Since the deviations between the predicted and tested ΔT in Shot 1 and Shot 2 are both less than 15%, it can be confidently claimed that the steep drop is caused by the tensile wave reflected by water surface.

Besides, the steep drop cannot be observed at P2 and P3 in Shot 1 and Shot 2 since the reflection from the pool bottom reaches the measuring points P2 and P3 earlier than the tensile wave, and induces minor peaks in the overpressure-time histories which is mixed with the cut-off effect. Besides, due to the existence of caisson, the overpressure recorded in
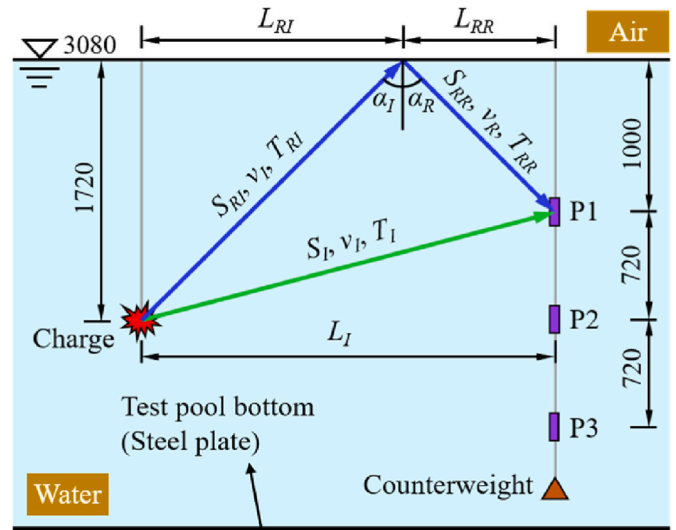

Fig. 10. Schematic of the geometric relationship (unit: mm).

Shot 3 and Shot 4 is relatively complex under the combined influences of multiple reflections, leading to the imperceptible exhibition of cut-off effect in the overpressure-time histories.
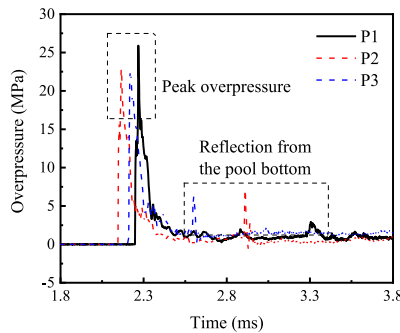
Based on the above analyses, it can be drawn that the water surface is of great significance in underwater explosion. For instance, the overpressure in shallow water is affected by the water surface, which is likely to yield negative pressure, and the underwater explosion loading can hardly transmit through the water surface nor cast impact in air.
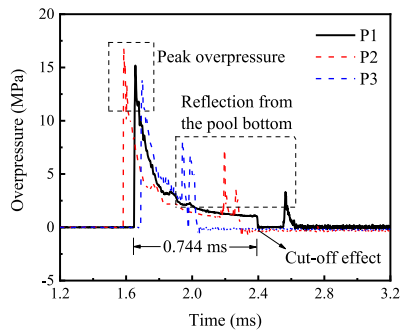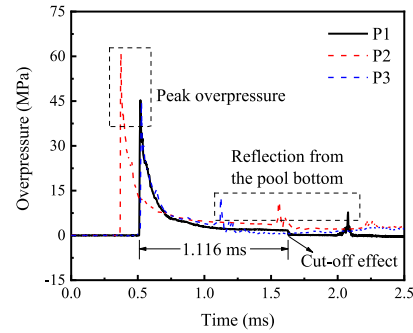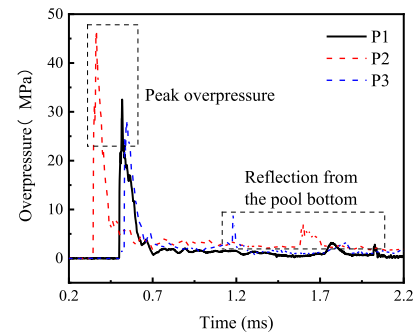

Fig. 9. Cut-off effect in (a) Shot 1 (b) Shot 2 (c) Shot 3 (d) Shot 4.

Table 2
Calculation of cut-off effect in the test (unit: m, ms).

Shot	S_I	v_I	T_I	S_{R1}	S_{R2}	v_R	$T_R = T_{RI} + T_{RR}$	$\Delta T = T_R\text{-}T_I$		Deviation (%)
								Calculation	Test	
Shot 1	3.085	1500	2.057	2.561	1.489	1498.5	2.701	0.644	0.744	−13.4
Shot 2	1.076	1500	0.717	1.793	1.042	1498.5	1.891	1.174	1.116	5.8

2.3. Dynamic behaviors of RC caisson specimen

Based on the underwater explosion loading characteristics clarified above, the dynamic behaviors of the caisson specimen in the test are further assessed in this section, and the experimental deflections of the front wall and damage pattern of caisson specimen are discussed.

2.3.1. Deflections of front wall

In Shot 3 and Shot 4, the deflections of the front wall were recorded by the displacement meters, and except for Shot 3-D2 due to the malfunction of the sensor, five valid deflection time-histories were obtained in the test and denoised by filtering with a 1000 Hz low-pass cut-off frequency, as shown in Fig. 11. It can be seen that the deflection-time histories show a fluctuating trend with several obvious peaks. Combined with the occurring time instants of peak overpressure and bubble oscillation shown in Fig. 4, it can be inferred that the first peaks in the deflection-time histories are attributed to the blast waves, while the following second and third ones are induced by bubble oscillations.

For Shot 3 ($Z = 2.71$ m/kg$^{1/3}$), the maximum deflection measured at D1 and D3 are 1.14 and 5.61 mm, and the corresponding residual deflections are −1.18 and 1.03 mm, respectively. For Shot 4 ($Z = 1.37$ m/kg$^{1/3}$), the maximum deflections measured at D1, D2 and D3 are 13.19, 42.16 and 32.85 mm, and the corresponding residual deflections are 1.02, 13.65 and 8.80 mm, respectively. Comparing the above two shots, the deflection data of Shot 4 is completely higher than that of Shot 3 due

to the larger charge weight and smaller standoff. Since the maximum deflection recorded in Shot 3 is less than 6 mm, taking account of the specimen dimension, it can be considered that the damage caused by Shot 3 hardly had an effect on the dynamic response of Shot 4. In addition, note that the blast wave and bubble oscillation induced the maximum deflections in Shot 3 and Shot 4, respectively. The reason for the different causes of the maximum deflections may lie in that, the larger scaled standoff in Shot 3 help the structure almost keep intact after the blast wave, and thus exhibiting slighter deflections under bubble oscillations. On the contrary, the smaller scaled standoff in Shot 4 accordingly caused the specimen to suffer non-negligible damage under the impact of blast wave, and reduced its blast-resistant capacity when facing the succeeding bubble oscillation.

Despite the absence of test data at Shot 3-D2, it can be generally concluded from Fig. 10 that the overall deflection of D1 is the smallest, followed by D3, while the data measured at D2 is the largest. Considering the position of three deflection measuring points, the reason for the discrepancy among deflections at different measuring points may lie in that: (i) since D1 is the farthest sensor away from the charge among all three measuring points, the underwater explosion loading acting on it should correspondingly be the mildest, resulting in the relatively smallest deflection; (ii) according to the analyses in Section 2.2, the underwater explosion loading can hardly be transmitted into air, and could possibly be reduced in shallow area attributed to the cut-off effect, thus the measuring point D1 which is adjacent to the water level may be
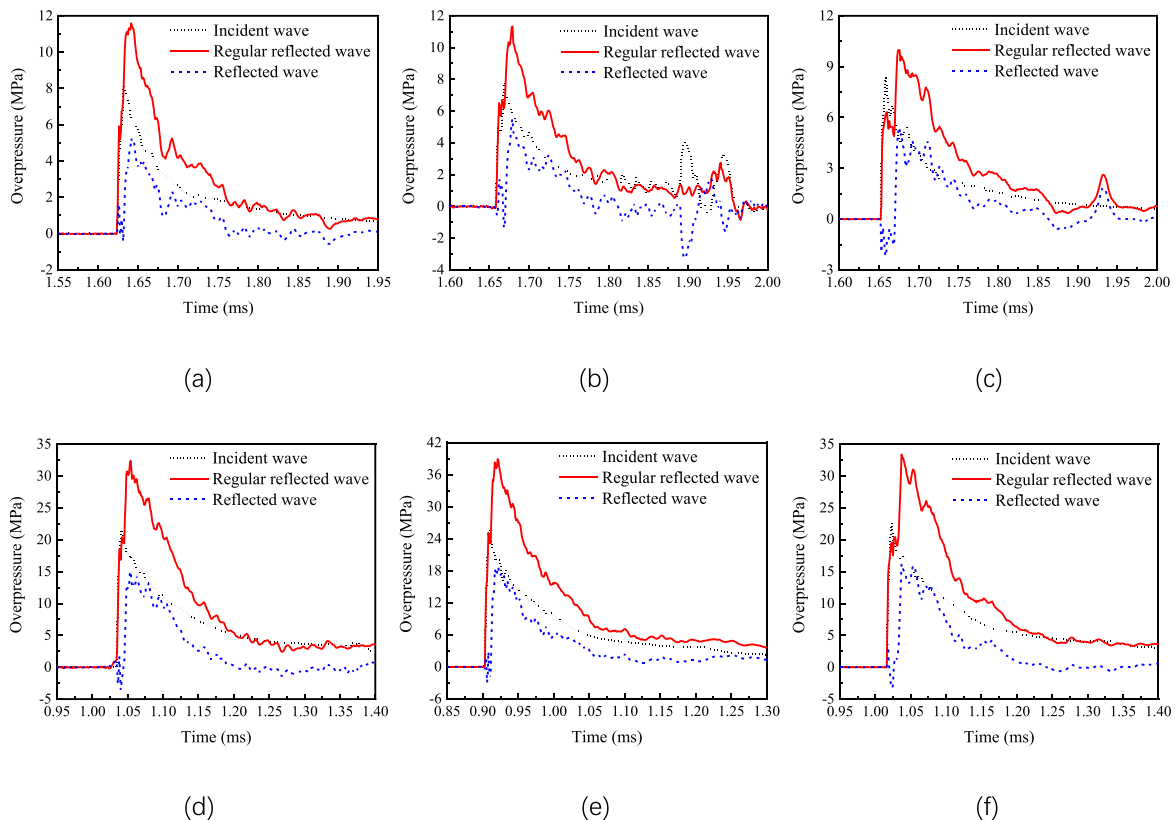

Fig. 11. Regular reflection wave of (a) Shot 1-P1 (b) Shot 1-P2 (c) Shot 1-P3 (d) Shot 2-P1 (e) Shot 2-P2 (f) Shot 2-P3 (Phase II).

less influenced by underwater explosions.

Besides, the negative residual deflection can be found in Shot 3-D1, which may relate to the following reasons: (i) the cut-off effect produced tensile stress in shallowly submerged area of caisson specimen, causing negative deflection at D1; (ii) since the charge was facing normally to D2 which was in the lower part of the caisson, the deflection near the bottom can yield an overturn moment and lead to a slight incline of the front wall; (iii) under the impact of underwater explosion, the water surged at the surface which could affect the deflection of D1.

2.3.2. Damage mode

After the test had been completed, the water was drained, and the caisson specimen was lifted out of the pool by cranes for examining the damaging pattern. As shown in Fig. 12, after enduring two consecutive underwater explosion shots, the caisson specimen is apparently damaged. The front wall suffered the most serious damage as evident vertical cracking is observed at the middle, while cracking and spalling of the concrete cover appear on the outside of the right chamber, which was faced with the charge. Meanwhile, slighter cracking shows up on the other side of the front wall, i.e., the outside of the left chamber shown in Fig. 12(a). For the inside of chamber, vertical cracks run through the midspan of the right chamber as shown in Fig. 12(b). Additionally, as seen in Fig. 12(a, c, d), the cracking and cratering can also be seen at where the front wall is connected to the bottom plate, side walls and partitions. Comparatively, the top plate is generally undamaged and kept intact with few cracks or spalling, as shown in Fig. 12(e). It should be noted that most of the damage is concentrated on the lower part of the specimen which was below the water level during the test, while the damage of the specimen above the water level can only be observed on the interior surface of the front wall as shown in Fig. 12(b).

Therefore, it can be concluded that: (i) for partially submerged structure subjected to underwater explosions, the structure above the water level is significantly less-damaged than that below the water level; (ii) most damage of the unsubmerged part of caisson against underwater explosion is caused by the influence of the overall response of the structure; (iii) for the components that are separated from the major structure and stay above the water level, e.g., the top plate, the underwater explosions cannot cause any serious damage.

3. Numerical simulations and comparisons

With the rapid development of computer technology and sophisticated analytical programs in the last several decades, numerical simulation has become an efficient supplement to the experimental tests. In this section, by adopting the FE program AUTODYN (Southpointe, 2020) with the Coupled Eulerian-Lagrangian algorithm and remapping technology, 1D and 3D models were established to reproduce the underwater explosion loadings and dynamic behaviors of caisson specimen, respectively.

3.1. FE models

In order to improve the computing efficiency and accuracy of numerical simulation, the remapping technology provided by AUTODYN is employed to apply the underwater explosion loading to the caisson. Fig. 13 gives the schematic of the remapping process. In detail, the charge is detonated in 1D FE model and computed until the blast wave front nearly passes through the explosion standoff *L*, and this distance gap is controlled within 50 mm at present. Then, the materials and the corresponding states (density, pressure, velocity, etc.) of water and TNT in 1D model at that exact moment are transferred into 3D FE model in a spatial axisymmetric manner. By remapping, the blast wave front in 3D model is about to reach the surface of the structure, thus the subsequent simulation can be efficiently carried out to predict the dynamic behaviors of caisson specimen. Generally, two FE models are involved in this section, i.e., the 1D model for predicting the underwater explosion loading and providing remapping files, and the 3D model for exploring the structural response.

As shown in Fig. 14(a), the 1D model is visually presented in a wedge-shape, while only the *X*-direction is involved in the simulation. The blast wave propagates underwater in a generally spherical shape with the charge as the center, and the 1D model actually performs mesh division and numerical simulation on the radius of the sphere, which can greatly reduce the mesh number and effectively avoid the deviations caused by the shape difference between the hexahedron mesh and the spherical blast wave in 3D model. The *Euler, Multi-material* solver is adopted, and the 1D model is correspondingly filled with water and TNT according to the equivalent radius of spherical charge. By preliminary simulation and analysis, the mesh size and calculation domain dimension are selected as 1/25 and 1000 times of the spherical charge radius R_0, respectively.
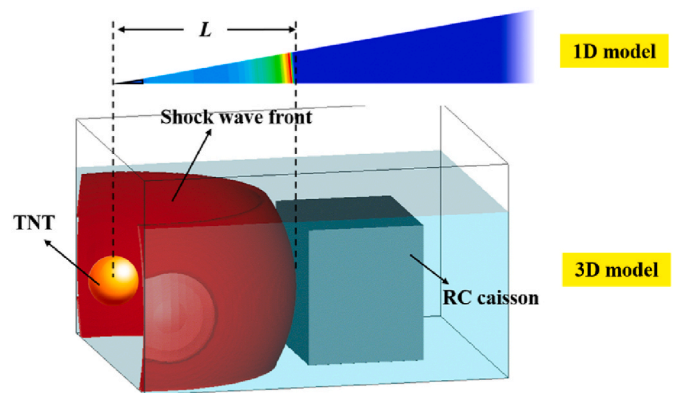

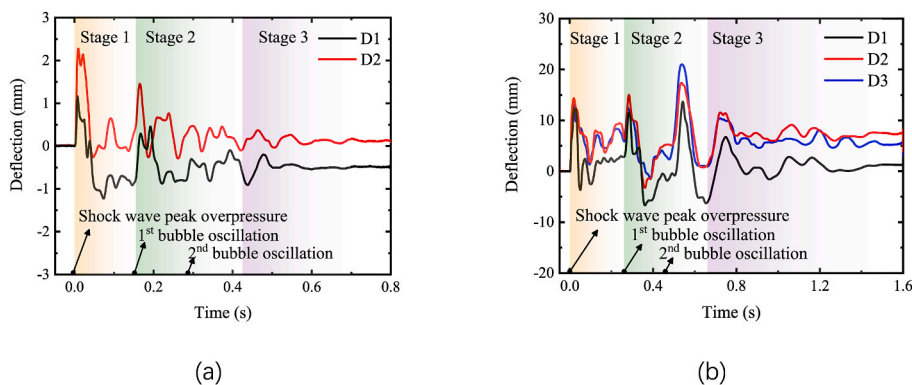**Fig. 13.** Schematic of remapping process.

(a)

(b)

Fig. 12. Deflection-time histories of (a) Shot 1 (b) Shot 2 (Phase II).
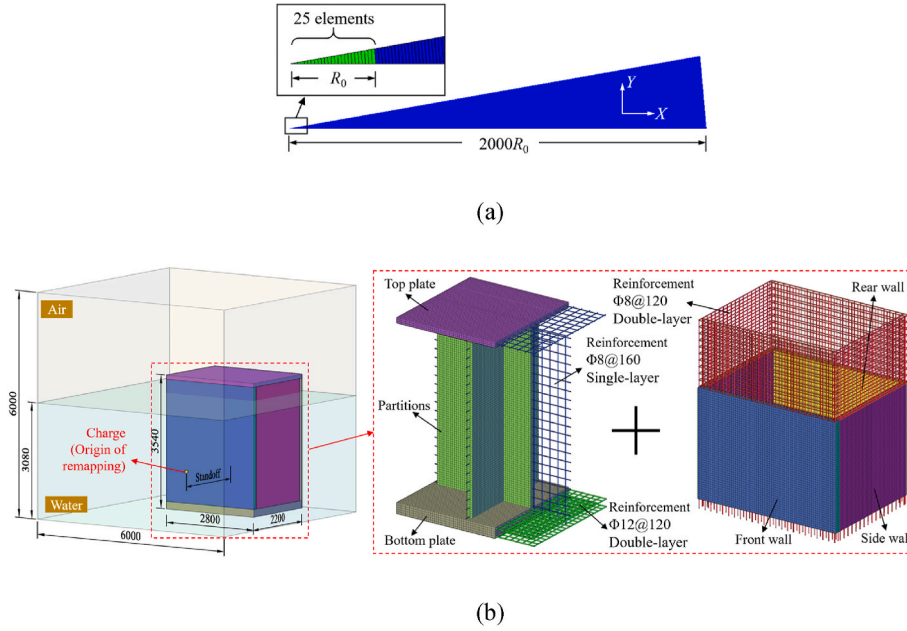
Fig. 14. FE models of underwater explosion test (a) 1D model (b) 3D model.

The 3D model used to predict the structural response is shown in Fig. 14(b). The configuration and detailing of the caisson model are consistent with the specimen in the present test (Fig. 2), in which the *beam* solver is adopted for reinforcement and *Lagrange* solver for concrete, and the mesh size is selected as 40 mm by trial and error. The concrete parts of the caisson are joined together except for the top plate, and the reinforcement is face-bonded with concrete. To reproduce the constraints of the pool side and bottom in the test, two vertical edge on the back side of the caisson is fixed through a boundary condition that restrains the velocity in X and Y directions, and the similar boundary condition which restrains the velocity in Z direction is utilized on the underside surface of the bottom plate. Additionally, a boundary condition of downward pressure is applied on the top plate to reflect the payload of surcharge. For the fluid part (air, water and TNT) in the 3D model, the *Euler, Multi-material* solver is adopted, and the air is filled into the corresponding volume according to the water level after remapping. Since the *Euler, Multi-material* solver only supports the hexahedron domain, the fluid part is set in a box-shape which can completely cover the caisson, charge and bubble oscillation with the mesh size of 40 mm due to preliminary trial results. The default reflection boundary is employed for the bottom and back side of the fluid part to simulate the side and bottom of the test pool, and the flow-out boundary is adopted for the remaining surfaces.

3.2. Material models and parameters

3.2.1. Fluid materials

The fluid in the model includes water, TNT and air. Since the water is commonly assumed to be incompressible, the polynomial equation of state (EOS) given in Eq. (5) is utilized. For TNT, the Jones-Wilkins-Lee (JWL) EOS is adopted, which has been widely used to calculate the high-energy explosions and the expansion of detonation products, as given in Eq. (6). Besides, the EOS of ideal gas is adopted for air as given in Eq. (7).

$$p = \begin{cases} A_1\mu + A_2\mu^2 + A_3\mu^3 + (B_0 + B_1\mu)\rho_0 e & \mu \geq 0 \\ T_1\mu + T_2\mu^2 + B_0\rho_0 e & \mu < 0 \end{cases} \tag{5}$$

where p is the pressure; $e = (\rho gh + p_0)/\rho B_0$ is the specific internal energy, which reflects the depth of burst; $\mu = \rho/\rho_0 - 1$ characterizes the compression, ρ and ρ_0 are the current and reference densities; A_1, A_2, A_3,

B_0, B_1, T_1 and T_2 are the corresponding constants.

$$p = A\left(1 - \frac{\omega\eta}{R_1}\right)e^{-\frac{R_1}{\eta}} + B\left(1 - \frac{\omega\eta}{R_1}\right)e^{-\frac{R_2}{\eta}} + \omega\eta\rho_0 e \tag{6}$$

where p is the pressure; e is the specific internal energy; $\eta = \rho/\rho_0$; A, B, ω, R_1 and R_2 are the corresponding constants.

$$p = (\gamma - 1)\rho e \tag{7}$$

where p is the pressure; ρ is the density; e is the specific internal energy; γ is the Adiabatic exponent taking the value of 1.4 for air.

3.2.2. Solid materials

The material model for concrete utilized in the simulation is the Riedel-Hiermaier-Thoma (RHT) model proposed by Riedel et al. (1999), which is a combined plasticity and shear damage model, and suitable for describing brittle materials under intensive loadings, e.g., impact and blast. The elastic, fracture and residual failure surfaces of RHT model are defined in Eqs. 8–10, as schematically shown in Fig. 15(a).

$$Y_{fail} = Y_{TXC}R_3F_{rate} \tag{8a}$$

$$Y_{TXC} = f_c\left[A\left(p^* - p_{spall}^*F_{rate}\right)^N\right] \tag{8b}$$

$$R_3 = \frac{2\left(1 - Q_2^2\right)\cos\theta}{4\left(1 - Q_2^2\right)\cos^2\theta + (2Q_2 - 1)^2}$$
$$+ \frac{(2Q_2 - 1)\left[4\left(1 - Q_2^2\right)\cos^2\theta + 5Q_2^2 - 4Q_2\right]^{1/2}}{4\left(1 - Q_2^2\right)\cos^2\theta + (2Q_2 - 1)^2} \tag{8c}$$

$$F_{rate} = \begin{cases} (\dot{\varepsilon}/\dot{\varepsilon}_0)^\alpha & p \geq f_c/3 \quad \dot{\varepsilon}_0 = 30 \times 10^{-6}s^{-1} \\ (\dot{\varepsilon}/\dot{\varepsilon}_0)^\delta & p < f_c/3 \quad \dot{\varepsilon}_0 = 3 \times 10^{-6}s^{-1} \end{cases} \tag{8d}$$

$$Y_{elastic} = Y_{fail}F_{elastic}F_{cap} \tag{9}$$

$$Y_{residual} = B(p^*)^M f_c \tag{10}$$

where Y_{fail}, $Y_{elastic}$ and $Y_{residual}$ are the fracture, elastic and residual failure surfaces, respectively; Y_{TXC} is the compressive meridian; R_3 is the third invariant dependence term; F_{rate} is a function of strain rate $\dot{\varepsilon}$; f_c is the
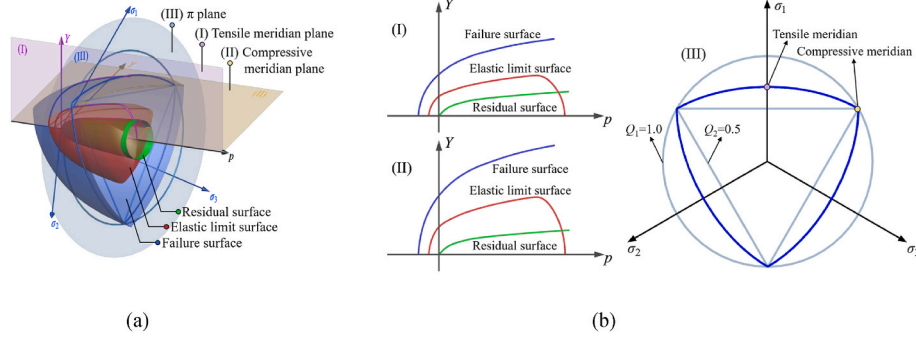
Fig. 15. RHT model (a) failure surfaces (b) meridian and π plane (Riedel et al., 1999).

compressive strength; A is the failure surface constant and N is the failure surface exponent; p^* is the pressure normalized with respect to f_c; $p^*_{spall} = p^*(f_t/f_c)$ is the normalized hydrodynamic tensile limit; θ is the lode angle; $Q_2 = Q_{2.0} + BQ \cdot p^*$ is the deviatoric stress ratio of failure curve at the tensile to compressive meridian on the deviatoric plane, and Fig. 15(b) gives the tensile and compressive meridian on the stress π plane; α and δ are the compressive and tensile strain rate factors, respectively; $F_{elastic}$ is the ratio of elastic strength to failure strength; F_{cap} is the limitation of elastic deviatoric stress under hydrostatic compression; B and M are the constant and exponent of residual failure surface, respectively.

The damage and strength reduction emerge as the additional plastic strain develops, which is accumulated due to inelastic deviatoric strain as formulated in Eq. (11). The failure surface and shear modulus of the post-damage stage is interpolated by Eq. (12) and Eq. (13), respectively. Additionally, the minimum failure strain ε_f^{min} is defined as 0.0008.

$$D = \sum \frac{\Delta \varepsilon_p}{\varepsilon_p^{failure}} = \sum \frac{\Delta \varepsilon_p}{D_1 \left(p^* - p^*_{spall}\right)^{D_2}} \tag{11}$$

$$Y^*_{fracture} = (1-D)Y^*_{failure} + DY^*_{residual} \tag{12}$$

$$G_{fracture} = (1-D)G + DG_{residual} \tag{13}$$

where D is the damage; $\Delta \varepsilon_p$ is increment of plastic strain; $\varepsilon_p^{failure}$ is the plastic strain when the material reaches the failure strength; G is the initial shear modulus; D_1 and D_2 are the corresponding constants.

For the steel reinforcement, Johnson-Cook (JC) model (Johnson and Cook, 1983) is employed, which is often chosen for simulating metallic materials enduring large strains and high strain rates, and the yield stress Y can be expressed as

$$Y = \left(A + B\varepsilon_p^n\right)\left(1 + C \ln \dot{\varepsilon}_p^*\right)\left(1 - T_H^m\right) \tag{14}$$

where ε_p^n is the effective plastic strain; $\dot{\varepsilon}_p^*$ is normalized effective plastic strain rate; $T_H^m = (T - T_{room})/(T_{melt} - T_{room})$ is the homologous temperature, where T_{room} and T_{melt} refer to room temperature and meting temperature, respectively.

Table 3 lists the parameter values of the above-mentioned material models adopted in the present simulations.

3.3. Comparisons

In this section, the above FE models and parameters are adopted to simulate the underwater explosion scenarios in the present test, and the prediction results, e.g., the overpressure- and deflection-time histories, as well as the damage patterns of caisson specimens are compared with the test data to examine the effectiveness of the FE analysis approach.

Table 3
Parameters of material models and EOS.

Symbol	Definition	Value	Symbol	Definition	Value
Water (Polynomial EOS)					
A_1	Bulk Modulus (kPa)	2.2×10^6	A_2	Compressive constant (kPa)	9.54×10^6
A_3	Compressive constant (kPa)	1.457×10^7	B_0	Compressive constant	0.28
B_1	Compressive constant	0.28	T_1	Tensile constant (kPa)	2.2×10^6
T_2	Tensile constant (kPa)	0	ρ_0	Reference density (kg/m³)	1.0×10^3
TNT (JWL EOS)					
A	Pressure constant (kPa)	3.712×10^8	B	Pressure constant (kPa)	3.231×10^6
ω	Fractional part of normal Tait equation adiabatic exponent	0.3	R_1	Principal eigenvalue	4.15
R_2	Secondary eigenvalue	0.95	ρ_0	Reference density (kg/m³)	1.6×10^3
Concrete (RHT model)					
f_t/f_c	Normalized tensile strength	0.1	f_s/f_c	Normalized shear strength	0.18
A	Intact failure surface constant	1.6	N	Intact failure surface exponent	0.61
BQ	Brittle to ductile transition	0.0105	$Q_{2.0}$	Tensile meridian ratio/ Compressive meridian ratio	0.6805
M	Fracture strength exponent	0.8	B	Fracture strength constant	0.7
δ	Tensile strain rate exponent	0..036	α	Compressive strain rate exponent	0.032
D_2	Damage constant	1.0	D_1	Damage constant	0.015
G	Initial shear modulus (kPa)	1.67×10^7	ρ	Reference density (kg/m³)	2.75×10^3
Steel (JC model)					
A	Initial yield stress (kPa)	4.92×10^5	B	Hardening constant (kPa)	5.1×10^5
n	Hardening exponent	0.26	C	Strain rate constant	0.014
m	Thermal softening exponent	1.03	T_{melt}	Melting temperature (K)	1.793×10^3
ρ	Reference density (kg/m³)	7.83×10^5	G	Initial shear modulus (kPa)	8.18×10^7

3.3.1. Underwater explosion loadings

The numerical simulations of the two shots in the free field, i.e., Shot 1 and Shot 2, were performed, and the corresponding comparisons of underwater explosion overpressure- and impulse-time histories are shown in Fig. 16. Since the measuring points P1 and P3 are at the same
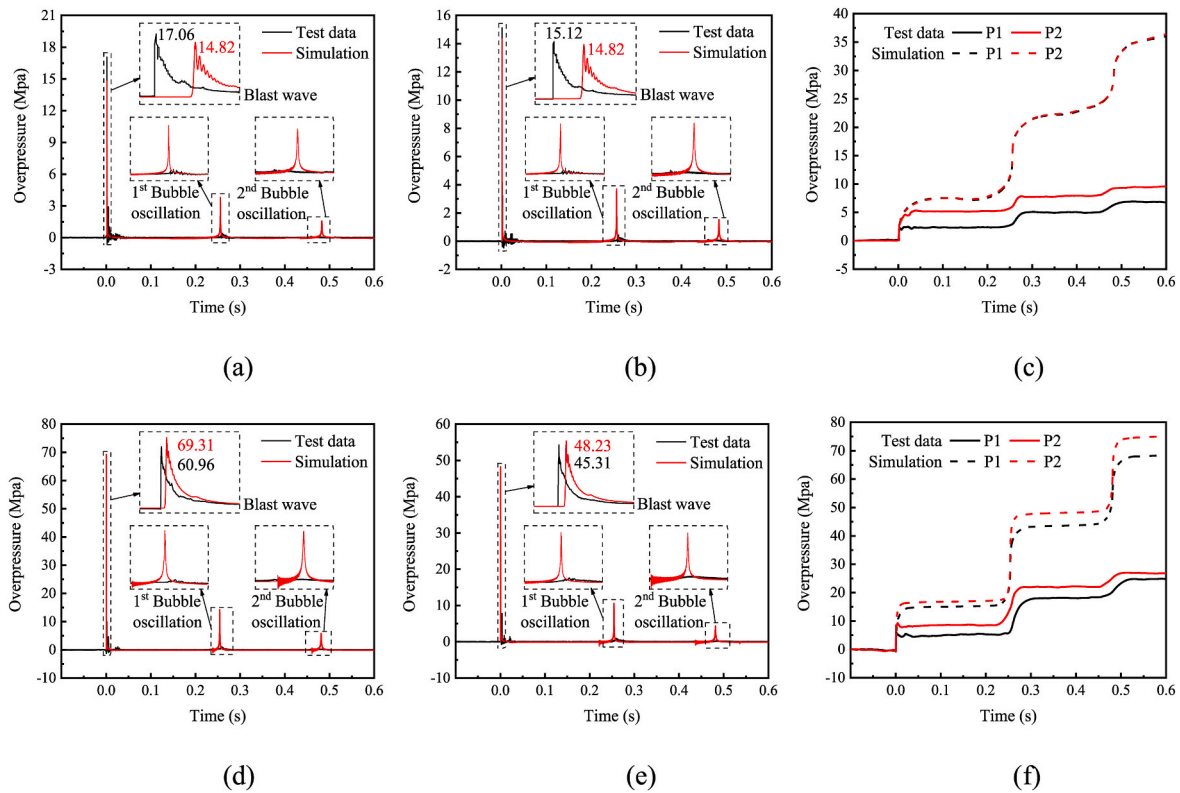
Fig. 16. Comparisons of time histories (a) Shot 1-P1 (b) Shot 1-P2 (c) Shot 1-impulse (d) Shot 2-P1 (e) Shot 2-P2 (f) Shot 2-impulse.

scaled standoffs, their predicted results of underwater explosion loading characteristics in 1D simulation should be identical. Therefore, P1 is taken to represent the measuring points at corresponding scaled standoffs for the comparisons. It can be seen that the predicted peak overpressures are in good agreement with the test data with the maximum deviation of 13.71%. Additionally, considering the influence of inevitable error in the test, the predicted peak overpressures are compared with the highly recognized formula for incident peak overpressure, i.e., Eq. (1). Better consistency is obtained with the absolute values of deviation at all measuring points in the two shots of free field test between 0.39% and 3.2%. It should be noted that though the bubble oscillation periods obtained from the test and numerical simulation are close, the predicted overpressure values of bubble oscillation are remarkably larger than the measured data. The above deviations may be attributed to the fact that the explosion energy cannot correctly dissipate in 1D FE simulation, while the free water surface in the test allows the escape of explosion energy from the water domain.

For the explosion impulse, the predicted results are obviously higher than the test data, which is possibly caused by the following reasons: (i) the bubble oscillation overpressure of numerical simulation in Fig. 16(a, b, d, e) is larger than test data due to the retaining energy, leading to the higher integral, i.e., impulse; (ii) as mentioned above, since the test results of impulse-time histories are integrated from the baseline-adjusted overpressure data, the accuracy of exact value cannot be precisely guaranteed; (iii) as discussed in Section 2.2.2, the equivalent spherical charge was adopted in the simulation which may show higher impulse than the group charge utilized in the test. However, the stepped manner observed in the test results is also clearly reflected in the simulation, and the occurring time instant of each significant increment, which represents the bubble oscillation, is very close to the experimental results. Thus, it can be considered that the present numerical simulation of underwater explosion loading has an acceptable credibility in terms of peak overpressure and bubble oscillation period. Nevertheless, the higher bubble oscillation overpressure and impulse demand for further

validation of both the 1D model and the corresponding FE analysis approach to examine its reliability on the predicted dynamic responses.

3.3.2. Dynamic behaviors of RC caisson

To further examine the reliability of both 1D and 3D models, as well as the corresponding FE analysis approach, the dynamic behaviors of caisson specimen subjected to the underwater explosion in Shot 3 and Shot 4 were numerically studied by utilizing the remapping files provided by 1D simulation and 3D model.

Taking Shot 3 for example, the comparisons of underwater explosion overpressure-time histories on the specimen are shown in Fig. 17. It can be seen that the predicted peak overpressures and bubble oscillations in Shot 3 are in good agreement with the test data. It should be pointed out that, the prediction accuracy of bubble oscillation overpressure is significantly improved by comparing to the 1D simulation result in Fig. 16. The reason may lie in that the flow-out boundary condition applied in the 3D model enables the dissipation of explosion energy in the water domain. For the predicted impulse, the overall growth trend is consistent with the test data. Besides, the simulated overpressure-time histories show more tiny random fluctuations compared to the test data, which is possibly caused by the computing error of CEL algorithm for the contact between the water and caisson.

Fig. 18 shows the comparisons of the predicted deflection-time histories with the test data. It indicates that the peak deflections and the corresponding occurring time instants are basically consistent, and the simulated first peak deflections induced by blast wave show good agreements with the test data. However, it can be seen that the second peak deflections at Shot 3-D1 appear to be different between the test data and simulation result. It is because that the negative deflection at Shot 3-D1 caused by the forward inclining trend affects the reflection of the second peak deflection in the test data, while the strict boundary conditions in the numerical simulation suppresses the emergence of forward inclining, and therefore clearly presents the second peak deflection. Besides, it can be found from Shot 4 that, the second peak
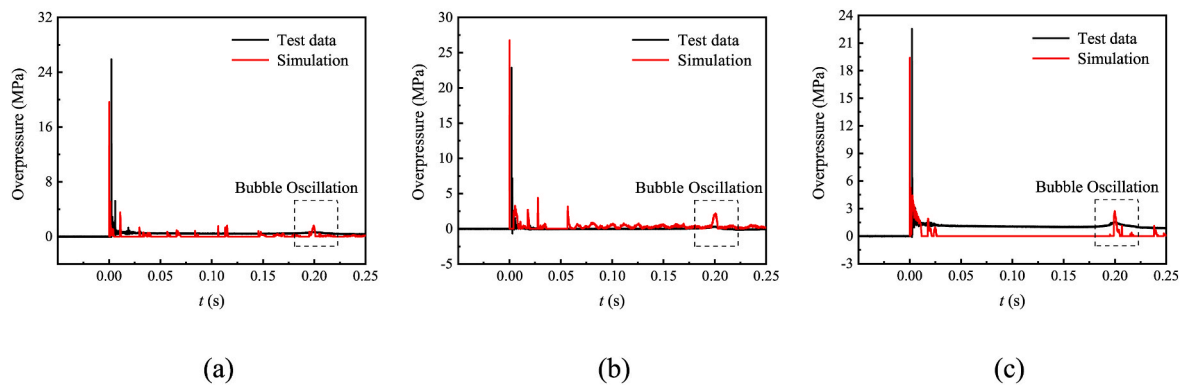
Fig. 17. Comparisons of overpressure-time histories (a) Shot 3-P1 (b) Shot 3-P2 (c) Shot 3-P3.
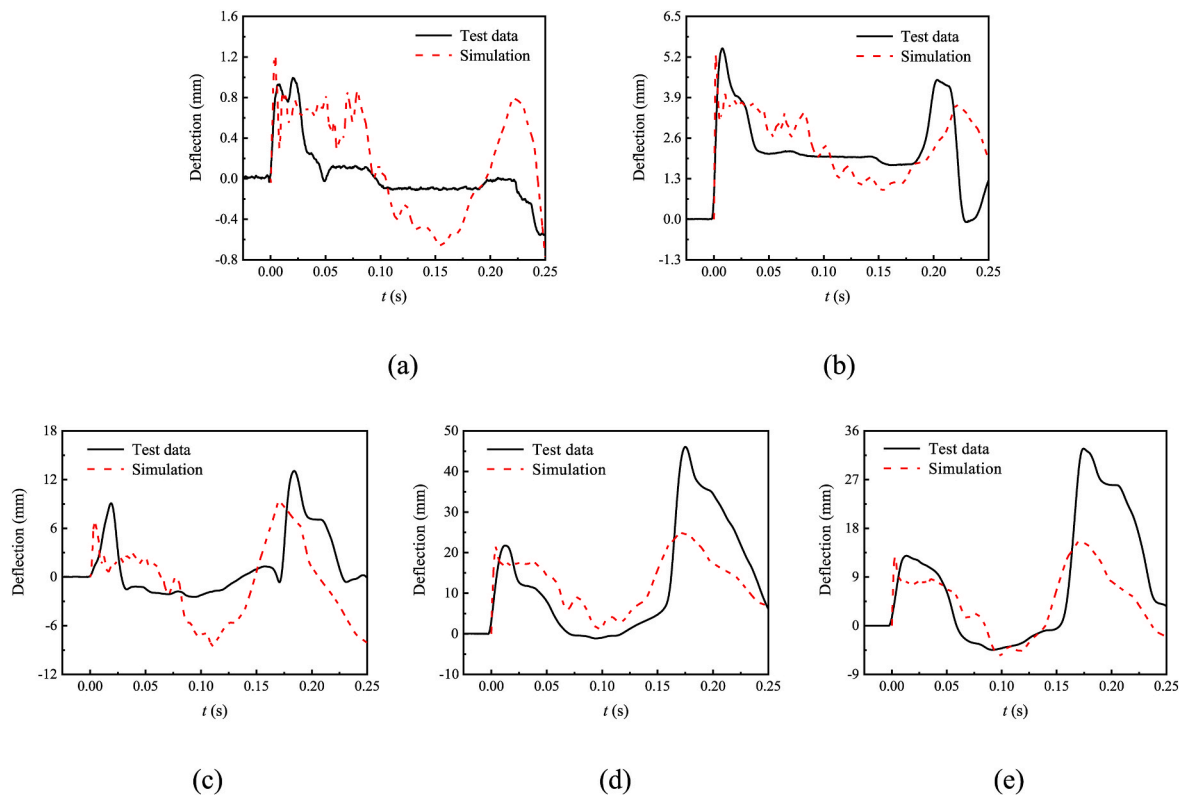

Fig. 18. Comparisons of deflection-time histories (a) Shot -3-D1 (b) Shot 3-D3 (c) Shot 4-D1 (d) Shot 4-D2 (c) Shot 4-D3.

deflection caused by bubble oscillation is underestimated by numerical simulation, which is possibly due to the fact that the two consecutive shots result in certain initial damage of caisson specimen in Shot 4 and accordingly deteriorate its response. Nevertheless, it still can be considered that the numerical simulation can basically reproduce the dynamic response of caisson, since the predicted results successfully reproduce the relationship between the first and second peak deflections, i.e., the first peak deflection is larger than second one in Shot 3, and the converse in Shot 4, which has been explained in Section 2.3.1.

The damage evolutions of caisson specimens under two shots are further illustrated in Fig. 19. It can be seen that, the failure first occurs at the middle of the front wall, and then quickly developed around the connections of the front wall to the bottom plate and side walls of the submerged part of caisson, while the top plate is barely influenced. Meanwhile, the evident damage occurs at the vertical edges on the rear side, which represents the contact between the specimen and the pool side. Compared with the damage pattern observed in the test (Fig. 11),

acceptable consistency can be seen between the predicted results and the test data.

Generally, the comparisons between the predicted results and test data show that the present 1D and 3D FE models and parameters, as well as the FE analysis approach are reliable to reproduce both the underwater explosion loading characteristics and the dynamic behaviors of RC caisson.

4. Further discussions

In order to further explore the influence of different water levels on the dynamic behaviors of caisson subjected to underwater explosions, combined with the actual situation of caisson wharves, the numerical simulation is carried out under two supplementary scenarios of Shot 3, namely Shot 5 and Shot 6. The original scenario of Shot 3 is under the water level of 3.08 m and the caisson was partially submerged. The water level in Shot 5 is set at 3.54 m, which makes the top surface of the
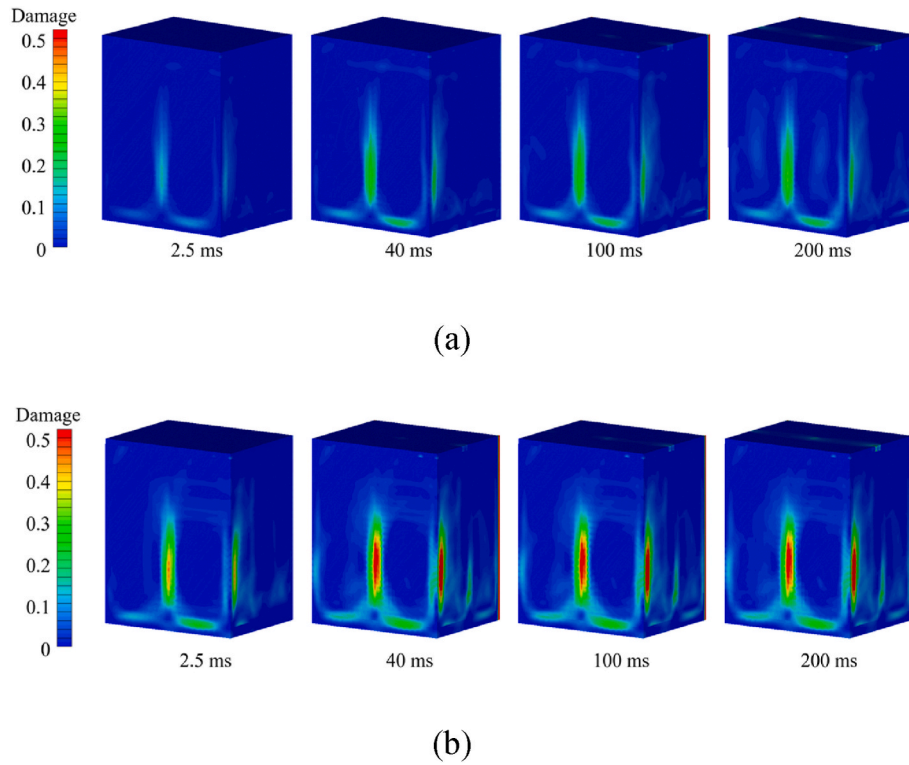
Fig. 19. Damage evolution of caisson in (a) Shot 3 (b) Shot 4.

caisson flush with the water surface. For Shot 6, the water level is set at 4 m, i.e., 460 mm higher than the top surface of the caisson which leads to a fully submerged caisson.

As mentioned above, the maximum deflection in Shot 3 is dominated by the blast wave. Therefore, in order to illustrate the differences in dynamic responses among Shot 3, Shot 5 and Shot 6, their deflection-time histories at blast wave stage are compared in Fig. 20. It can be seen that, the deflections in Shot 5 and Shot 6 are overall significantly larger than that in Shot 3. Specifically, at measuring point D1, the maximum deflection obviously increases as the water level rises. For the measuring points D2 and D3, the maximum deflections in Shot 5 and Shot 6 are very close and both remarkably larger than that in Shot 3. The results show that, (i) the dynamic response of partially submerged caissons is considerably smaller than that of fully submerged caissons; (ii) the change of water level influences more on the structural part adjacent to the water surface; (iii) for the deep-submerged part which is far from the water surface, the influence of water level changing is small when the caisson is fully submerged.

The terminal damage patterns of caisson in Shot 3, Shot 5 and Shot 6

are given in Fig. 21. For partially submerged caisson (Shot 3), the damage is mainly concentrated in the lower part, and the top plate remains intact. For Shot 5, the water surface is flush with the top surface of caisson, and minor damage can be observed on the top plate. The damage occurs in a larger range on the fully submerged caisson (Shot 6), and it can be seen that the top plate suffers more serious damage compared to Shot 3. The results show that the water level cast a significant impact on the dynamic behaviors of caisson subjected to underwater explosions. Generally, fully submerged caissons suffer more damage than partially submerged caissons, especially for superstructures.

5. Conclusions

The influence of water level on RC caisson subjected to underwater explosions was studied experimentally and numerically, mainly focusing on the underwater explosion loading characteristics and dynamic behaviors of caisson. Based on four shots of field underwater explosion test concerning the free field and a partially submerged caisson specimen, as
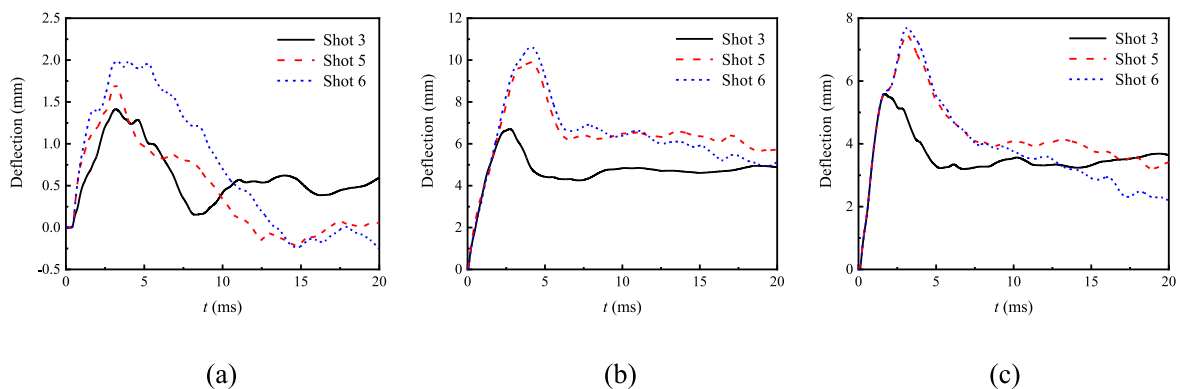

Fig. 20. Comparisons of deflection-time histories at (a) D1 (b) D2 (c) D3.
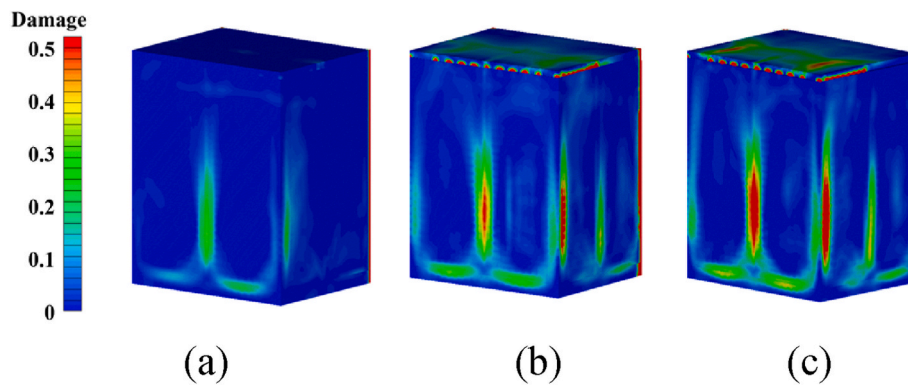
Fig. 21. Terminal damage patterns of caisson in (a) Shot 3 (b) Shot 5 (a) Shot 6.

well as the numerical simulations with adopting 1D and 3D FE models. The main conclusions can be drawn as follows:

(1) Derived based on the spherical charge, Cole's formula for underwater explosion peak overpressure is also applicable to group charge, while Zamyshlyaev's formula for underwater explosion impulse induced by blast wave leads to overestimations for group charge scenarios.

(2) The impulse-time history of underwater explosion shows in a stepped manner with remarkable increase at the preceding blast wave and the succeeding bubble oscillations, which implies that the bubble oscillation is of great importance to underwater explosion loading.

(3) For partially submerged caisson subjected to underwater explosions, the unsubmerged part of caisson suffers less damage than the submerged part, hence the superstructures of RC caisson are under preferable protection when subjected to underwater explosions.

(4) The upper part of caisson exhibits higher sensitivity to the change of water level. The rise of water level intensifies the dynamic response of caisson subjected to underwater explosions, especially for upper part near the water surface; the lower part submerged deeply in the water is less affected by the change of water level once the caisson is fully submerged.

(5) The partially submerged caisson shows slighter damage than fully submerged caisson, which indicates that a larger height of the caisson should be considered when performing underwater blast-resistant design, and more rigorous detailing should be applied to caissons apt to be fully submerged, e.g., higher concrete strength and reinforcement ratio.

CRediT authorship contribution statement

Y. Zhang: Designing the test, Writing – original draft. **Y.D. Zhou:** Performing the test and numerical simulations, Writing – original draft. **H. Wu:** Supervising and reviewing the entire work, Funding acquisition, Polishing and editing the text.

Declaration of competing interest

The authors declare that they have no known competing financial interests or personal relationships that could have appeared to influence the work reported in this paper.

Data availability

No data was used for the research described in the article.

Acknowledgement

References

Ben-Dor, G., 1992. Shock Wave Reflection Phenomena. Springer, Berlin.

Cole, R.H., 1948. Underwater Explosion. Dover Publication Inc., New York.

Dong, Q., Wei, Z.B., Tang, T., Li, L.F., Liu, J.H., 2019. Damage effects of caisson gravity wharf under underwater explosion. Explos. Shock Waves 39 (6), 113–123 (in Chinese).

Geers, T.L., Hunter, K.S., 2002. An integrated wave-effects model for an underwater explosion bubble. Acoustical Soc. Am. 111 (4), 1584–1601.

Gu, W.B., Zheng, Z.P., Liu, J.Q., Li, D.J., Lu, M., 2006. Experimental investigation of the oblique collision effects of explosion shock wave on concrete frustum in shallow water. Explos. Shock Waves 4, 75–80 (in Chinese).

Huang, X.P., Kong, X.Z., Hu, J., Fang, Q., 2022a. Failure modes of concrete gravity dam subjected to near-field underwater explosion: centrifuge test and numerical simulation. Eng. Fail. Anal. 137, 106243.

Huang, X.P., Hu, J., Zhang, X.D., Zhang, Z.T., 2022b. Effect of bubble pulse on concrete gravity dam subjected to underwater explosion: centrifuge test and numerical simulation. Ocean Eng. 243, 110291.

Hung, C.F., Lin, B.J., Hwangfu, J.J., Hsu, P.Y., 2009. Dynamic response of cylindrical shell structures subjected to underwater explosion. Ocean Eng. 36 (8), 564–577.

Johnson, G.R., Cook, W.H., 1983. A constitutive model and data for metals subjected to large strains, high strain rates and high temperatures. In: Proceedings of the 7th International Symposium on Ballistics, pp. 541–546. The Hague, Netherlands.

LeBlanc, J., Shukla, A., 2011. Dynamic response of curved composite panels to underwater explosive loading: experimental and computational comparisons. Compos. Struct. 93 (11), 3072–3081.

Li, Q., Wang, G.H., Lu, W.B., Niu, X.Q., Chen, M., Yan, P., 2018. Failure modes and effect analysis of concrete gravity dams subjected to underwater contact explosion considering the hydrostatic pressure. Eng. Fail. Anal. 85, 62–76.

Li, S.M., Zhang, A.M., Cui, P., 2020. Study on the interaction between the bubble and free surface close to a rigid wall. Acta Aerodyn. Sin. 38 (4), 796–806.

Liu, J.H., 2002. Theory and its Applications of Ship Dynamic Responses to Non-contact Underwater Explosions. China Ship Scientific Research Center, Wuxi, pp. 22–40 (in Chinese).

Liu, J.H., Tang, T., Wei, Z.B., Dong, Q., Li, L.F., 2020. Damage effects of a caisson wharf subjected to underwater contact explosion. Explos. Shock Waves 40 (11), 111407 (in Chinese).

Murata, K., Takahashi, K., Kato, Y., 2004. Underwater shock and bubble pulse loading against model steel cylinder. In: International Symposium on Explosion, Shock Wave and Hypervelocity Phenomena (ESHP Symposium), pp. 283–287. Kumamoto, Japan.

Rajendran, R., Narasimhan, K., 2006. Deformation and fracture behavior of plate specimens subjected to underwater explosion-a review. Int. J. Impact Eng. 32 (12), 1945–1963.

Riedel, W., Thoma, K., Hiermaier, S., Schmolinske, E., 1999. Numerical analysis using a new macroscopic concrete model for hydrocodes. In: Proceedings of 9th International Symposium on Interaction of the Effects of Munitions with Structures, pp. 315–322. Berlin, Germany.

Rolfe, E., Quinn, R., Irven, G., Brick, D., Dear, J.P., Arora, H., 2020. Underwater blast loading of partially submerged sandwich composite materials in relation to air blast loading response. Int. J. Lightweight Mater. Manufac. 3 (4), 387–402.

Snay, H.G., 1956. Hydrodynamics of underwater explosions. In: Symposium on Naval Hydrodynamics. National Academy of Sciences, Washington, D.C., pp. 325–352

Southpointe, 2020. ANSYS Explicit Dynamics Analysis Guide. ANSYS, Inc., Canonsberg, PA.

Taylor, G.I., 1963. The Pressure and Impulse of Submarine Explosion Waves on Plates. The Scientific Papers of G. I. Taylor. Cambridge University Press, Cambridge, pp. 287–303.

Tian, S.Z., Du, X.L., Yan, Q.S., Wu, J., Zhuang, T.S., 2021. Damage effect of pile wharf under underwater explosion load. Mech. Adv. Mater. Struct. https://doi.org/10.1080/15376494.2021.2006840.

Wang, L.L., 2005. Foundation of Stress Waves. National Defense Industry Press, Beijing (in Chinese).

Yan, Q.S., Liu, C., Wu, J., Wu, J., Zhuang, T.S., 2020. Experimental and numerical investigation of reinforced concrete pile subjected to near-field non-contact underwater explosion. Int. J. Struct. Stabil. Dynam. 20, 2040003, 06.

Yang, G.D., Wang, G.H., Lu, W.B., Zhao, X.H., Yan, P., Chen, M., 2019. Cross-section shape effects on anti-knock performance of RC columns subjected to air and underwater explosions. Ocean Eng. 181, 252–266.

Zamyshlyaev, B.V., Yakovlev, U.S., 1967. Dynamic Loads in Underwater Explosion. Shipbuilding, Leningrad (in Russian).

Zhao, X.H., Wang, G.H., Lu, W.B., Yan, P., Chen, M., Zhou, C.B., 2018. Damage features of RC slabs subjected to air and underwater contact explosions. Ocean Eng. 147, 531–545.

Zhuang, T.S., Wang, M.Y., Wu, J., Yang, C.Y., Zhang, T., Gao, C., 2020. Experimental investigation on dynamic response and damage models of circular RC columns subjected to underwater explosions. Defense Technol. 16 (4), 856–875.